Lawrence Berkeley National Laboratory

Title
Note on numerical study of the beam energy spread in NDCX-I

Permalink
https://escholarship.org/uc/item/5rw1g083

Author
Vay, J.-L.

Publication Date
2011-06-30

Note on numerical study of the beam energy spread in NDCX-I

by
J.-L. Vay, P.A. Seidl, and A. Friedman

from
Lawrence Berkeley National Laboratory (on behalf of U.S. HIFS-VNL)
1 Cyclotron Road, Berkeley, CA 94720
Accelerator Fusion Research Division
Berkeley, California 94720
and
Lawrence Livermore National Laboratory

January 19, 2011

Note on numerical study of the beam energy spread in NDCX-I

J.-L. Vay, P.A. Seidl, A. Friedman

(Dated: 19 January 2011)

The kinetic energy spread (defined here as the standard deviation of the beam particle energies) sets the ultimate theoretical limit on the longitudinal compression that can be attained on NDCX-I and NDCX-II. Experimental measurements will inevitably include the real influences on the longitudinal phase space of the beam due to injector and accelerator field imperfections[1]. These induced energy variations may be the real limit to the longitudinal compression in an accelerator. We report on a numerical investigation of the energy spread evolution in NDCX-I; these studies do not include all the real imperfections, but rather are intended to confirm that there are no other intrinsic mechanisms (translaminar effects, transverse-longitudinal anisotropy instability, etc.) for significant broadening of the energy distribution.
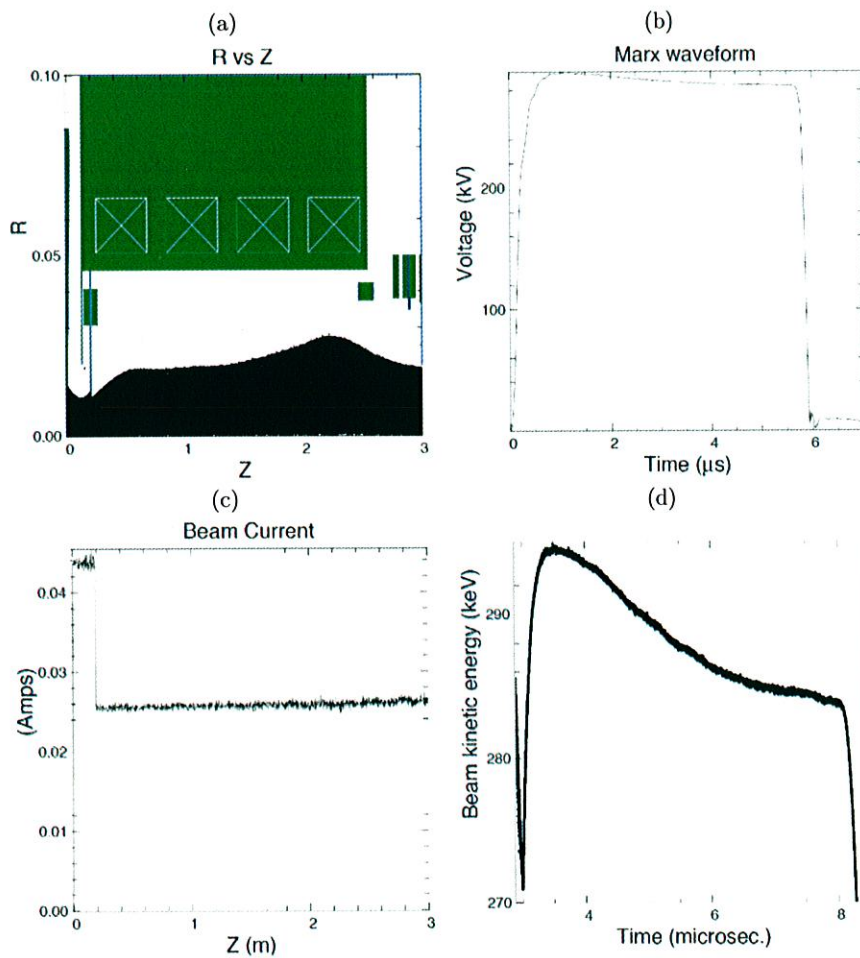

FIG. 1. From a Warp simulation of NDCX-I (snapshots taken at t=4μs), (a) snapshot of the beam (black) and lattice (green), (b) Marx waveform, (c) snapshot of beam current, (d) kinetic energy history by of beam macroparticles hitting the end plate at $z = 3$ m.

We have performed Warp simulations that use a realistic Marx voltage waveform which was derived from experimental measurements (averaged over several shots), a fully-featured model of the accelerating and focusing lattice, and new diagnostics for computing the local energy spread (and temperature) that properly account for linear correlations that arise from the discrete binning along each physical dimension (these capabilities reproduce and extend those of the earlier HIF code BPIC[2]; see Appendix I for more details). The new diagnostics allow for the calculation of multi-dimensional maps of energy spread and temperature in 2-D axisymmetric or 3-D Cartesian space at selected
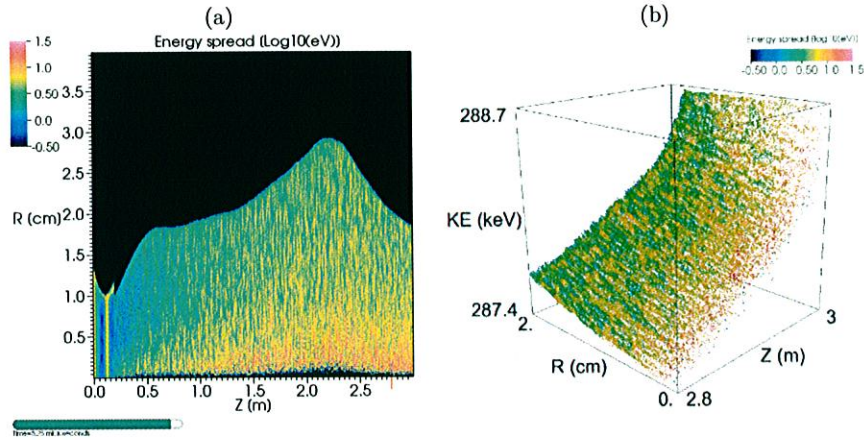
FIG. 2. From a Warp simulation of NDCX-I , (a) 2-D axisymmetric map of energy spread (in Log10(eV)); (b) scatter plot of kinetic energy versus radius and longitudinal position (0.28 m< z < 3 m) colored according to local energy spread.
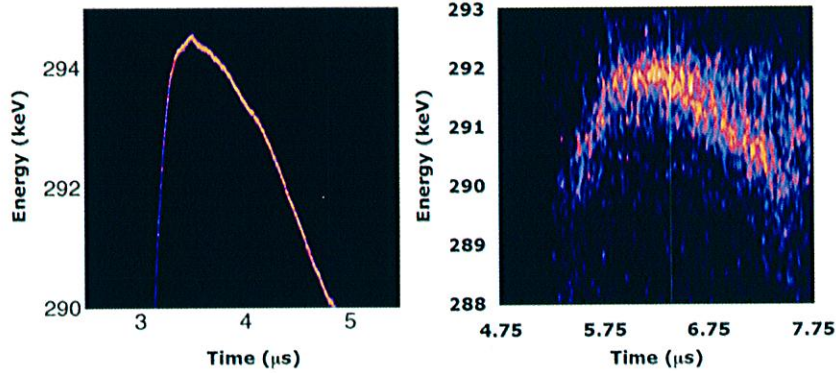

FIG. 3. NDCX-I beam energy history from (left) Warp simulation; (right) NDCX-I measurement using a spectrometer and a streak camera.

times. The simulated beam-line was terminated at z = 3 m by a conducting plate, so as to approximately reproduce the experimental conditions at the entrance of the spectrometer that was used for mapping the longitudinal phase space.

Snapshots of the beam projection and current, as well as the Marx waveform and history of beam kinetic energy collected at the end plate, are shown in Fig. 1. A two-dimensional axisymmetric map of energy spread from simulations of a typical NDCX-I configuration is shown in Fig. 2 (a). The energy spread starts at 0.1 eV at the source and rapidly rises to a few eV, then fluctuates between a fraction of an eV and tens of eV, ending near the exit in a range of a few eV at the outer edge of the beam to a few tens of eV near the axis. The higher value on-axis is associated with greater numerical noise there, due to the axisymmetric geometry of the calculation, resulting in poorer simulation-particle statistics at small radius. A scatter plot of the macroparticles kinetic energy (KE) versus radius (R) and longitudinal position (0.28 m< z < 3 m) colored by local energy spread is shown in Fig. 2 (b). As expected, there is a correlation of the kinetic energy with radius that is clearly visible at $z = 2.8$ m and vanishes at the metal plate at $z = 3$ m. More snapshots from simulations varying the time step, grid resolution and number of macroparticles are given in Appendix II.

The macro-particles were collected at the exit plate and their kinetic energy history is plotted in Fig. 3 (left) and contrasted to an experimental measurement using a streak camera shown in Fig. 3 (right) (taken from [1]). For some types of measurements, averaging over several pulses to improve signal-to-noise will contribute an additional spread that may not be present on any single beam pulse [1]. The upper bound for the energy spread is in the range of a few 100 eV for the experiment while in the range of a few eV for the reported Warp simulations. The Marx voltage exhibits variations in the range of up to several hundreds of volts, playing a significant role in the experimentally measured energy spread, which may account for the difference between the experimental and the simulated bounds.

APPENDIX A - CALCULATION OF THE TEMPERATURE AND ENERGY SPREAD IN WARP

Assuming a distribution of particles $f(X, V)$ of positions $X = \{x, y, z\}$ and velocities $V = \{v_x, v_y, v_z\}$, the temperature kT_u along the direction $u = x$, y or z and the kinetic energy spread δK at $X_0 = \{x_0, y_0, z_0\}$ are defined as being directly related respectively to the variance of the velocity components and the standard deviation of the kinetic energy as:

$$kT_u = \frac{1}{2}m\overline{(v_u - \overline{v_u})^2} = \frac{1}{2}m\frac{\int_{-\infty}^{\infty} f(X_0, v_u)(v_u - \overline{v_u})^2 \cdot dv_u}{\int_{-\infty}^{\infty} f(X_0, v_u) \cdot dv_u} \tag{1}$$

$$\delta K = \sqrt{\overline{(K - \overline{K})^2}} = \frac{1}{2}m\sqrt{\frac{\int_0^{\infty} f(X_0, V)(K - \overline{K})^2 \cdot dK}{\int_0^{\infty} f(X_0, V) \cdot dK}} \quad , \tag{2}$$

where m, $v = \sqrt{v_x^2 + v_y^2 + v_z^2}$ and $K = \frac{1}{2}mv^2$ are respectively the mass, velocity and kinetic energy of the particles, and the mean values of the velocity components and kinetic energy are given by

$$\overline{v_u} = \frac{\int_{-\infty}^{\infty} f(X_0, v_u) v_u \cdot dv_u}{\int_{-\infty}^{\infty} f(X_0, v_u) \cdot dv_u} \tag{3}$$

$$\overline{K} = \frac{\int_0^{\infty} f(X_0, V) K \cdot dK}{\int_0^{\infty} f(X_0, V) \cdot dK} \quad . \tag{4}$$

The above definitions apply to infinitesimal volumes and continuous density functions f and can be interpreted as the mathematical limit of discretized equivalent definitions for a finite size sample of N particles and finite volumes $\delta\Omega$ when $N \to \infty$ and $\delta\Omega \to 0$. At these limits, correlations between velocity (or kinetic energy) with position vanish and do not need to appear explicitly in the calculation of temperature or energy spread. In practice, however, both N and $\delta\Omega$ are finite, and correlations need eventually to be accounted for.

As an example, we consider a snapshot from a simulation of NDCX-I. The longitudinal phase space $z - v_z$ is plotted in Fig. 4-(a) for $0 < z < 1\text{m}$, while a small sample for $5 \text{ cm}< z < 5.1$ cm and 6.4 mm$< r < 7.7$ mm is shown in Fig. 4-(b), and with averages removed in Fig. 4-(c). A linear correlation is clearly visible, which would give rise to an overestimate of the local temperature if not removed. The sample with linear correlation removed is shown in Fig. 4-(d).

Removing the linear correlations necessitates the knowledge of the correlation coefficients for each spatial direction, which are computed as follows.

Let us assume that at $X_0 = \{x_0, y_0, z_0\}$, the kinetic energy $K_1 = K - \overline{K}$ has a linear correlation with the sample positions x, y and z, such that $K_1 = K_2 + a_1x_1 + b_1y_1 + c_1z_1$ where $x_1 = x - \overline{x}$, $y_1 = y - \overline{y}$, $z_1 = z - \overline{z}$, $\overline{x_1K_2} = \overline{y_1K_2} = \overline{z_1K_2} = 0$, and a_1, b_1 and c_1 are scalars giving the "slopes" of the coupling in each spatial direction. From the definitions given above, one can write

$$\overline{x_1K_2} = \overline{x_1(K_1 - a_1x_1 - b_1y_1 - c_1z_1)} = 0 \tag{5}$$

$$\overline{y_1K_2} = \overline{y_1(K_1 - a_1x_1 - b_1y_1 - c_1z_1)} = 0 \tag{6}$$

$$\overline{z_1K_2} = \overline{z_1(K_1 - a_1x_1 - b_1y_1 - c_1z_1)} = 0 \tag{7}$$

such that a_1, b_1 and c_1 are the solutions of the linear system

$$\begin{cases} \overline{x_1^2}a_1 + \overline{x_1y_1}b_1 + \overline{x_1z_1}c_1 - \overline{x_1K_1} = 0 \\ \overline{y_1x_1}a_1 + \overline{y_1^2}b_1 + \overline{y_1z_1}c_1 - \overline{y_1K_1} = 0 \\ \overline{z_1x_1}a_1 + \overline{z_1y_1}b_1 + \overline{z_1^2}c_1 - \overline{z_1K_1} = 0 \end{cases} \quad . \tag{8}$$

The system is solved explicitly in Warp. The same procedure is used to remove linear correlations between v_x, v_y and v_z for the temperature calculations.

Although not present (or discernable) in the 1 mm sample that was shown, higher order correlations can be present, as shown in Fig. 5 for a 4 mm long sample, and should ideally be removed. In the present version of the Warp diagnostic, only the linear correlation is removed, as a compromise between accuracy and speed. In the future, the subroutine could be modified to recursively remove spatial correlations up-to an arbitrary order, as described below.
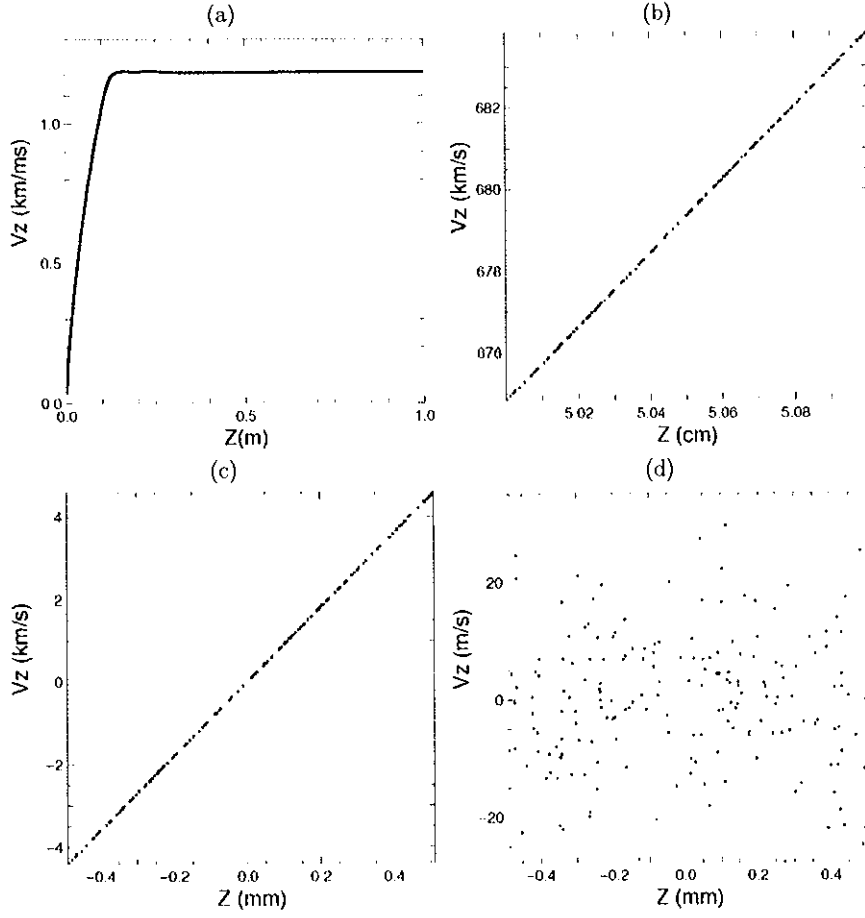
FIG. 4. Longitudinal $z - v_z$ phase-space projection from a simulation of NDCX-I for (a) $0 < z < 1$ m, (b) a small sample between 6.4 mm$< r < 7.7$ mm and 5 cm$< z < 5.1$ cm, (c) same sample as (b) with averages removed along z and v_z, (d) same sample as (c) with linear correlation between v_z and z removed.

More generally, one can write the kinetic energy distribution as the weighted sum of powers of x_1, y_1 and z_1 up to order n

$$K = K_{n+1} + \sum_{i=0}^{n} \left(a_i x_1^i + b_i y_1^i + c_i z_1^i + d_i \right) \tag{9}$$

while imposing $\overline{x^n K_{n+1}} = \overline{y^n K_{n+1}} = \overline{z^n K_{n+1}} = 0$ and $\overline{K_n} = 0$. The distribution K_{n+1} can be computed recursively using

$$K_{n+1} = K_n - a_n x_1^n - b_n y_1^n - c_n z_1^n - d_n \tag{10}$$

and solving for

$$\begin{cases} \overline{x_1^{2n}} a_n + \overline{x_1^n y_1^n} b_n + \overline{x_1^n z_1^n} c_n + \overline{x_1^n} d_n = \overline{x_1^n K_n} \\ \overline{y_1^n x_1^n} a_n + \overline{y_1^{2n}} b_n + \overline{y_1^n z_1^n} c_n + \overline{y_1^n} d_n = \overline{y_1^n K_n} \\ \overline{z_1^n x_1^n} a_n + \overline{z_1^n y_1^n} b_n + \overline{z_1^{2n}} c_n + \overline{z_1^n} d_n = \overline{z_1^n K_n} \\ \overline{x_1^n} a_n + \overline{y_1^n} b_n + \overline{z_1^n} c_n + d_n = 0 \end{cases} \tag{11}$$

We note that for n odd, then $\overline{x_1^n} = \overline{y_1^n} = \overline{z_1^n} = 0$, giving $d_n = 0$ and the system to solve simplifies to

$$\begin{cases} \overline{x_1^{2n}} a_n + \overline{x_1^n y_1^n} b_n + \overline{x_1^n z_1^n} c_n = \overline{x_1^n K_n} \\ \overline{y_1^n x_1^n} a_n + \overline{y_1^{2n}} b_n + \overline{y_1^n z_1^n} c_n = \overline{y_1^n K_n} \\ \overline{z_1^n x_1^n} a_n + \overline{z_1^n y_1^n} b_n + \overline{z_1^{2n}} c_n = \overline{z_1^n K_n} \end{cases} \tag{12}$$
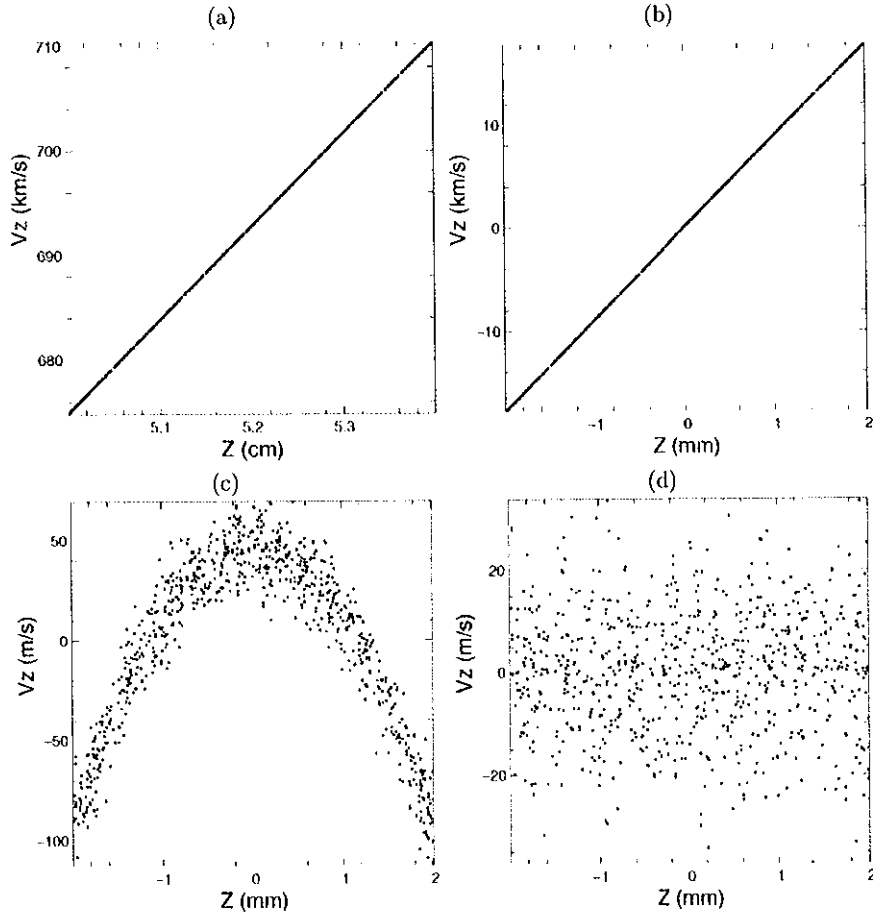
FIG. 5. Longitudinal $z-v_z$ phase-space projection from a simulation of NDCX-I for (a) a small sample between 6.4 mm$< r < 7.7$ mm and 5 cm$< z < 5.4$ cm, (b) same sample as (a) with averages removed along z and v_z, (c) same sample as (b) with linear correlation between v_z and z removed (d) same sample as (c) with quadratic correlation between v_z and z removed.

The recursive procedure that was just described has been applied successfully to the sample case shown in Fig. 5, for removing the quadratic correlation between v_z and z that is visible in Fig. 5-(c), giving the uncorrelated distribution plotted in Fig. 5-(d). Comparing Fig. 4-(d) and 5-(d) shows that removing higher order correlations allows for larger samples, reducing the size of the diagnostic arrays and improving the statistic per cell. This procedure will be implemented in Warp in the near future, adding the option of either setting a maximum level of recursion level (or equivalently highest order of correlation to be removed) or setting a tolerance for stopping the recursion on the difference between the temperature (or energy spread) value at two consecutive recursion levels. Sorting the macroparticle data by temperature (or energy spread) grid cells beforehand would allow for each cell to reach independent levels of recursion.

Finally, although this was not discussed here, the emitter region presents a near singularity which calls for finer sampling of the diagnostic. Thus, accurate and detailed calculation of energy spread and temperature near the source would benefit from adaptive mesh refinement (AMR) of the diagnostic grid near those singular regions. The AMR tools developed for field calculations may thus be of benefit for those diagnostics.

APPENDIX B - WARP SIMULATIONS OF NDCX-I VARYING NUMERICAL PARAMETERS

Snapshots of energy spread, longitudinal temperature, kinetic energy, and kinetic energy minus the slice average, are plotted from Warp simulations of NDCX-I for various numerical parameters:

- Fig. 6: $\delta x = \delta z = 2$ mm, $\delta t = 1.25$ ns, $N_p \approx 1.8$ million macroparticles,

- Fig. 7: $\delta x = \delta z = 2$ mm, $\delta t = 0.625$ ns, $N_p \approx 1.8$ million macroparticles,

- Fig. 8: $\delta x = 0.4$ mm, $\delta z = 1$ mm, $\delta t = 1.25$ ns, $N_p \approx 1.8$ million macroparticles,

- Fig. 9: $\delta x = \delta z = 2$ mm, $\delta t = 1.25$ ns, $N_p \approx 18$ million macroparticles,

- Fig. 10: $\delta x = 0.4$ mm, $\delta z = 1$ mm, $\delta t = 1.25$ ns, $N_p \approx 18$ million macroparticles.

From the limited set of numerical parameters that were involved, the following indications emerge: the energy spread and longitudinal temperature are not sensitive to the time step but are very sensitive to the resolution and the number of macroparticles. This suggests that numerical noise is contributing to unphysical heating and that the simulation with the highest resolution and number of macroparticles may not yet be converged. The usage of standard techniques for noise reduction (e.g. higher order particle shapes, filtering of charge density) should be considered for future simulations, with the caveat that care must be exercised near conductors (this may need some study and algorithm development). We finally note that despite the fact that convergence was not demonstrated on the highest resolution run, the upper bound that was obtained for energy spread is well below the one that has been obtained experimentally, and is thus deemed adequate for the present purpose.
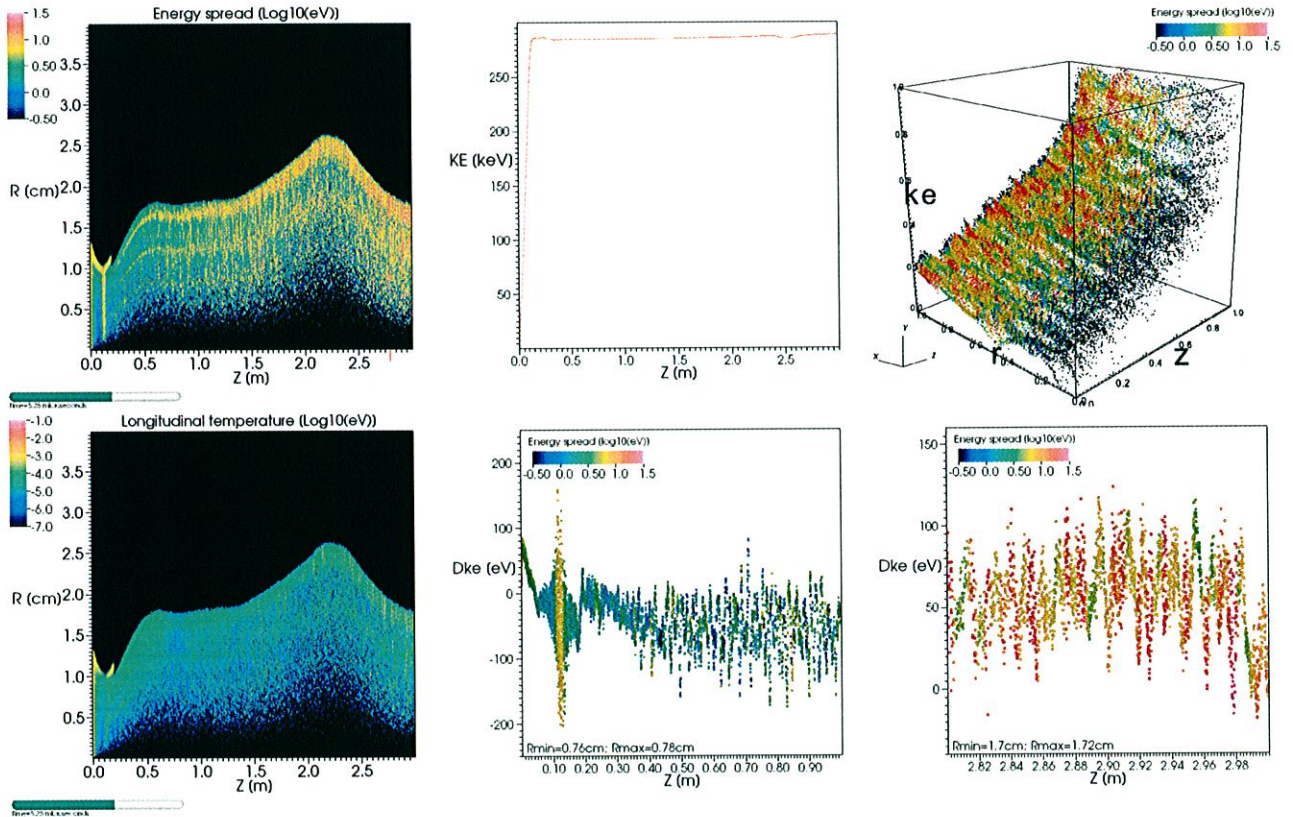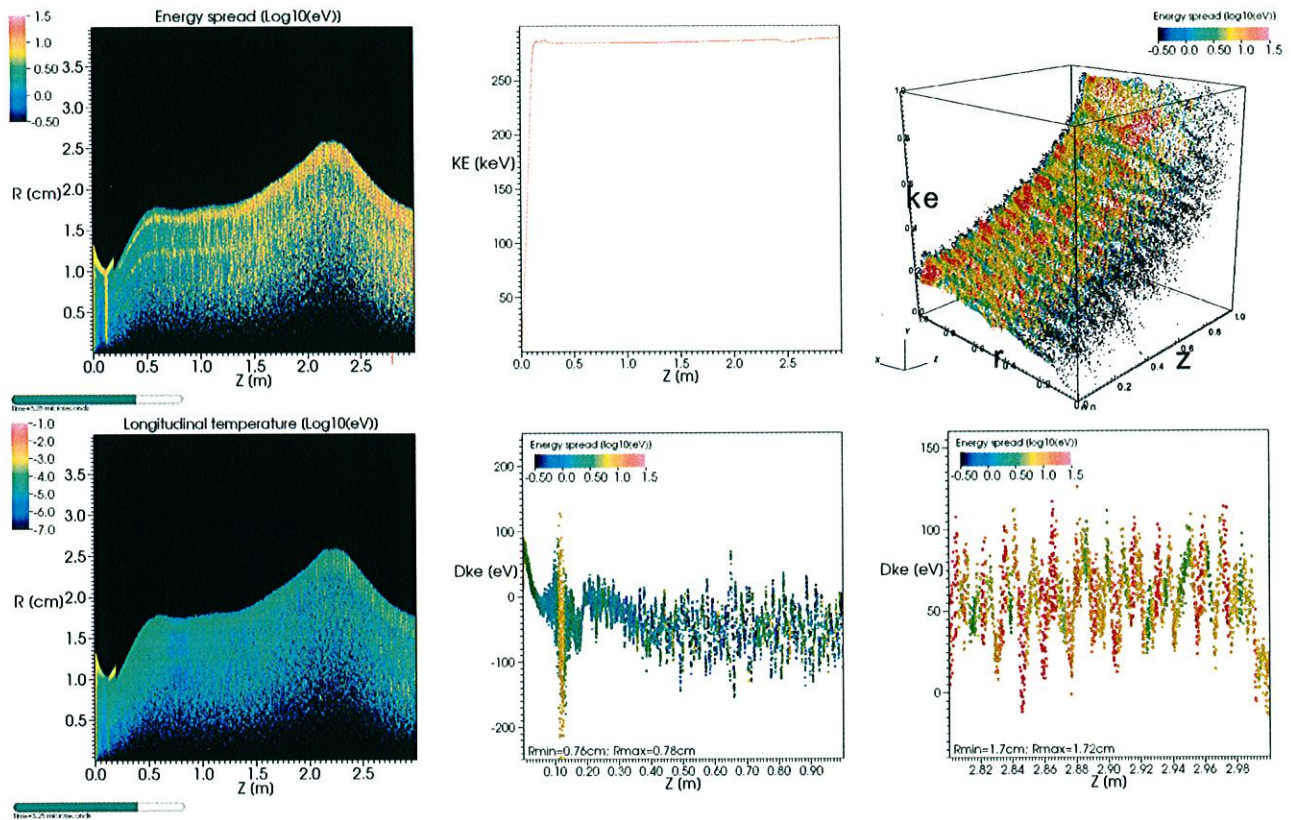

FIG. 6. From Warp simulation of NDCX-I with $\delta x = \delta z = 2$ mm, $\delta t = 1.25$ ns, $N_p \approx 1.8$ million macroparticles: snapshots of (top-left) beam kinetic energy spread vs (r,z); (top-middle) kinetic energy vs z; (top-right) kinetic energy vz (r,z), colored by energy spread for 2.8 m$< z <$ 3 m; (bottom-left) longitudinal temperature vs (r,z); (bottom-middle) kinetic energy minus averaged slice energy for $0 < z < 1$ m and a thin annulus 0.76 cm$< r <$ 0.78 cm, colored by energy spread; (bottom-right) same as (bottom-middle) but for 2.8 m$< z <$ 3 m and 1.7 cm$< r <$ 1.72 cm.

[1] J.E. Coleman, Ph.D. thesis, Berkeley, USA, 2008
[2] J.-L. Vay, Ph.D. thesis, Orsay, France, 1996

FIG. 7. From Warp simulation of NDCX-I with $\delta x = \delta z = 2$ mm, $\delta t = 0.625$ ns, $N_p \approx 1.8$ million macroparticles: snapshots of (top-left) beam kinetic energy spread vs (r,z); (top-middle) kinetic energy vs z; (top-right) kinetic energy vz (r,z), colored by energy spread for 2.8 m$< z <$ 3 m; (bottom-left) longitudinal temperature vs (r,z); (bottom-middle) kinetic energy minus averaged slice energy for $0 < z < 1$ m and a thin annulus 0.76 cm$< r <$ 0.78 cm, colored by energy spread; (bottom-right) same as (bottom-middle) but for 2.8 m$< z <$ 3 m and 1.7 cm$< r <$ 1.72 cm.
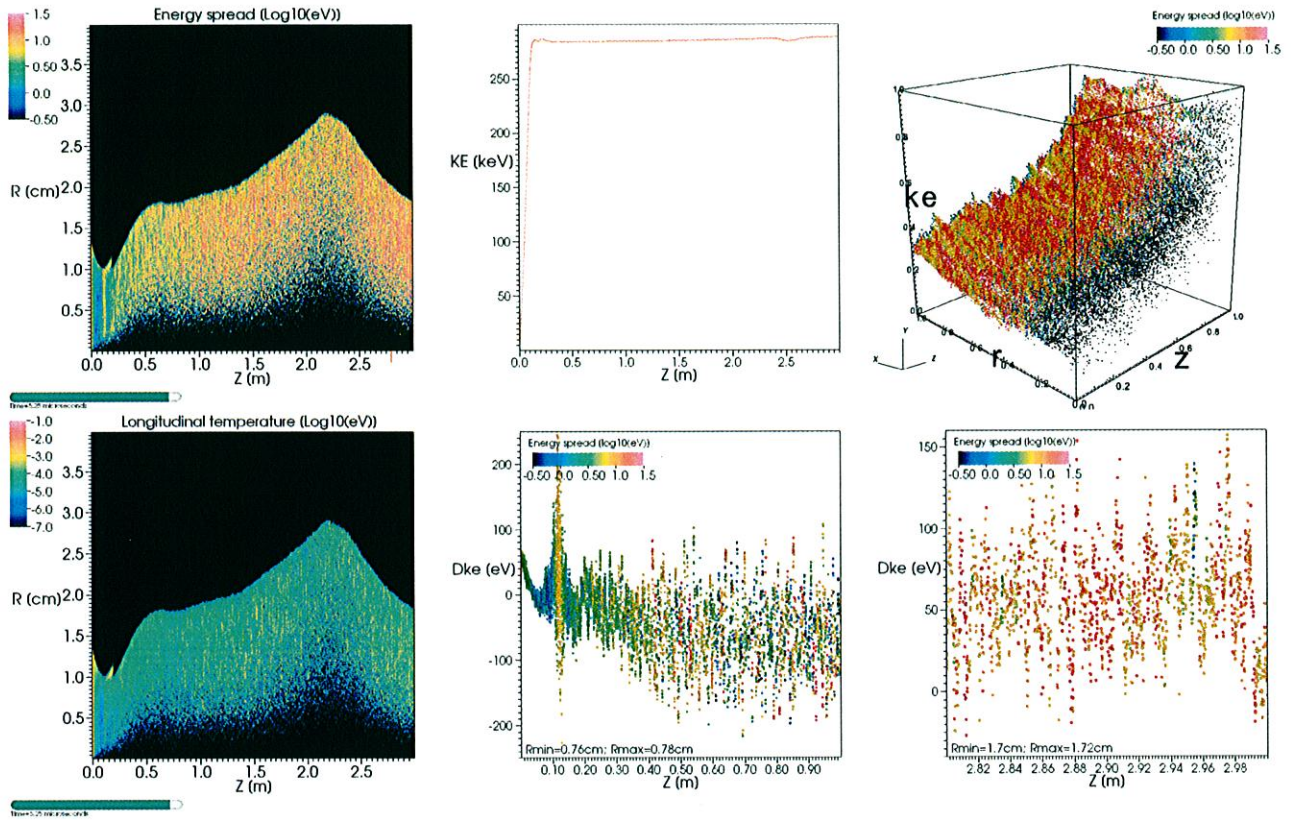
FIG. 8. From Warp simulation of NDCX-I with $\delta x = 0.4$ mm, $\delta z = 1$ mm, $\delta t = 1.25$ ns, $N_p \approx 1.8$ million macroparticles: snapshots of (top-left) beam kinetic energy spread vs (r,z); (top-middle) kinetic energy vs z; (top-right) kinetic energy vz (r,z), colored by energy spread for 2.8 m$< z <$ 3 m; (bottom-left) longitudinal temperature vs (r,z); (bottom-middle) kinetic energy minus averaged slice energy for $0 < z < 1$ m and a thin annulus 0.76 cm$< r <$ 0.78 cm, colored by energy spread; (bottom-right) same as (bottom-middle) but for 2.8 m$< z <$ 3 m and 1.7 cm$< r <$ 1.72 cm.
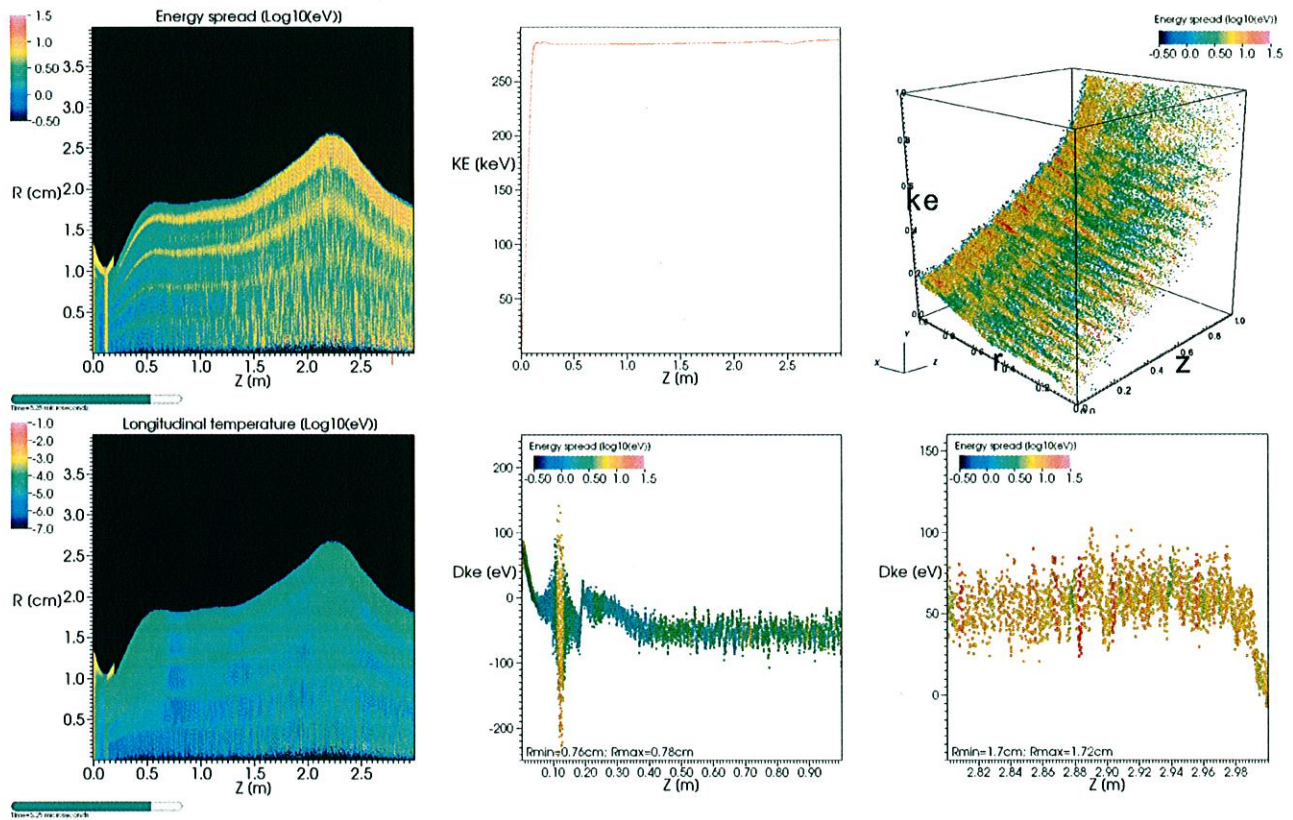
FIG. 9. From Warp simulation of NDCX-I with $\delta x = \delta z = 2$ mm, $\delta t = 1.25$ ns, $N_p \approx 18$ million macroparticles: snapshots of (top-left) beam kinetic energy spread vs (r,z); (top-middle) kinetic energy vs z; (top-right) kinetic energy vz (r,z), colored by energy spread for 2.8 m$< z <$ 3 m; (bottom-left) longitudinal temperature vs (r,z); (bottom-middle) kinetic energy minus averaged slice energy for $0 < z < 1$ m and a thin annulus 0.76 cm$< r <$ 0.78 cm, colored by energy spread; (bottom-right) same as (bottom-middle) but for 2.8 m$< z <$ 3 m and 1.7 cm$< r <$ 1.72 cm.
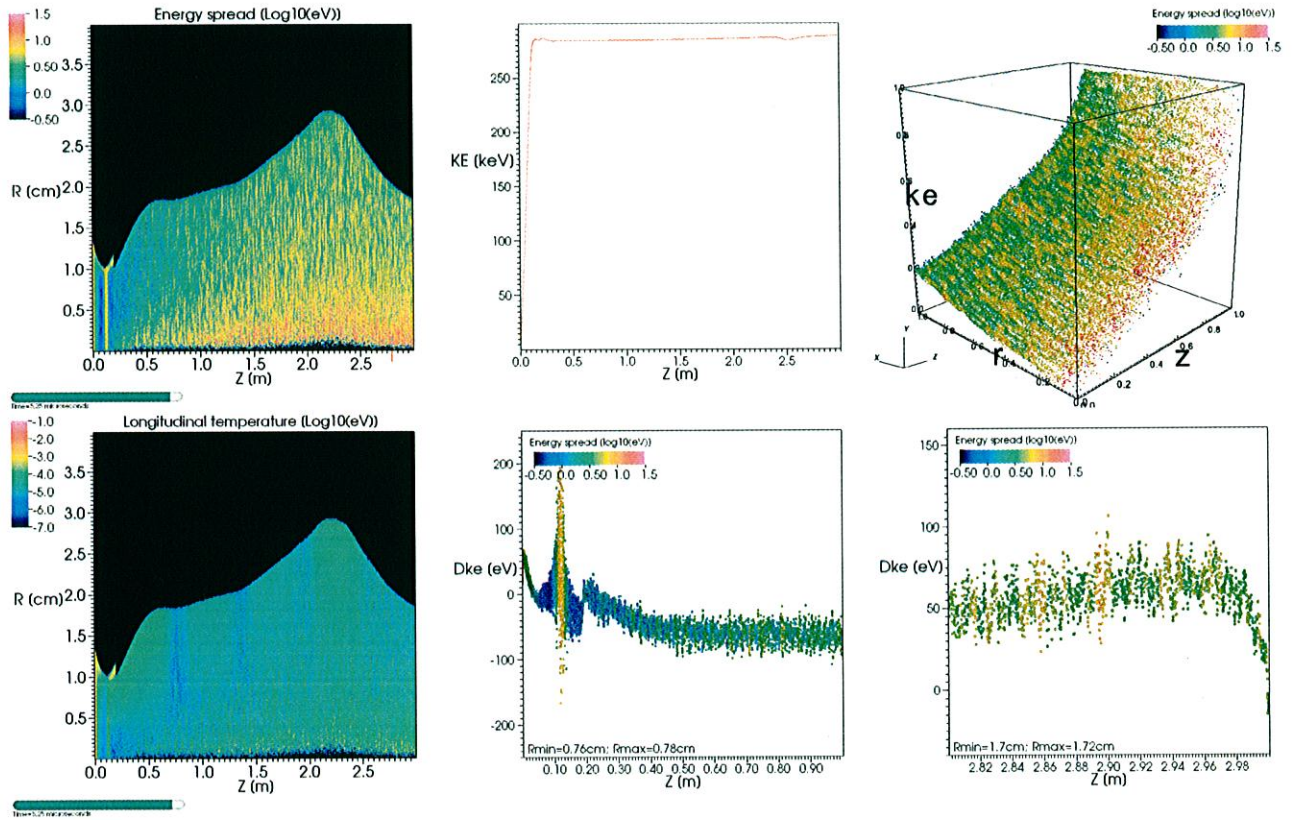
FIG. 10. From Warp simulation of NDCX-I with $\delta x = 0.4$ mm, $\delta z = 1$ mm, $\delta t = 1.25$ ns, $N_p \approx 18$ million macroparticles: snapshots of (top-left) beam kinetic energy spread vs (r,z); (top-middle) kinetic energy vs z; (top-right) kinetic energy vz (r,z), colored by energy spread for 2.8 m$< z <$ 3 m; (bottom-left) longitudinal temperature vs (r,z); (bottom-middle) kinetic energy minus averaged slice energy for $0 < z < 1$ m and a thin annulus 0.76 cm$< r <$ 0.78 cm, colored by energy spread; (bottom-right) same as (bottom-middle) but for 2.8 m$< z <$ 3 m and 1.7 cm$< r <$ 1.72 cm.